J. Fluid Mech. (2012), *vol.* 694, *pp.* 5–28.
doi:10.1017/jfm.2011.437

Buckling of a thin-layer Couette flow

Anja C. Slim[1], **Jeremy Teichman**[2] **and L. Mahadevan**[1]†

[1] Department of Physics and School of Engineering and Applied Sciences, Harvard University, 29 Oxford Street, Cambridge, MA 02138, USA

[2] Institute for Defense Analyses, Virginia, USA

(Received 3 March 2011; revised 2 October 2011; accepted 2 October 2011; first published online 24 November 2012)

We analyse the buckling stability of a thin, viscous sheet when subject to simple shear, providing conditions for the onset of the dominant out-of-plane modes using two models: (i) an asymptotic theory for the dynamics of a viscous plate, and (ii) the full Stokes equations. In either case, the plate is stabilized by a combination of viscous resistance, surface tension and buoyancy relative to an underlying denser fluid. In the limit of vanishing thickness, plates buckle at a shear rate $\gamma/(\mu d)$ independent of buoyancy, where $2d$ is the plate thickness, γ is the average surface tension between the upper and lower surfaces, and μ is the fluid viscosity. For thicker plates stabilized by an equal surface tension at the upper and lower surfaces, at and above onset, the most unstable mode has moderate wavelength, is stationary in the frame of the centreline, spans the width of the plate with crests and troughs aligned at approximately 45° to the walls, and closely resembles elastic shear modes. The thickest plates that can buckle have an aspect ratio (thickness/width) of approximately 0.6 and are stabilized only by internal viscous resistance. We show that the viscous plate model can only accurately describe the onset of buckling for vanishingly thin plates but provides an excellent description of the most unstable mode above onset. Finally, we show that, by modifying the plate model to incorporate advection and make the model material-frame-invariant, it is possible to extend its predictive power to describe relatively short, travelling waves.

Key words: low-Reynolds-number flows, materials processing flows, thin films

1. Introduction

Folding, buckling and coiling are phenomena frequently associated with thin elastic solids. However, they also occur in very viscous films and filaments whenever compression is faster than can be accommodated by film or filament thickening. Viscous buckling has been studied in a variety of contexts over the last half-century. A primary motivation for some of the earliest work was understanding the buckling of layered geological strata modelled as very viscous fluid layers (with viscosities that range from 10^{16} to 10^{21} Pa s). This work was pioneered by Biot (e.g. Biot 1961), who examined the two-dimensional, small-deformation folding of viscous layers embedded in a less viscous medium and subjected to layer-parallel compression. He used the Stokes–Rayleigh analogy relating viscous creeping flows with their elastic counterparts

† Email address for correspondence: lm@seas.harvard.edu

(Rayleigh 1945) and the concomitant similarity between elastic and viscous governing equations to develop expressions for the critical load and wavelength of the instability. Many subsequent studies (e.g. Ramberg 1963; Chapple 1968) added further physical effects (a summary is given by Johnson & Fletcher 1994). Viscous buckling is also encountered in more familiar contexts: the folding of cake batter pouring into a pan, the wrinkling of a layer of cream on hot milk, and the coiling of a stream of honey falling from a spoon. Each of these examples also has industrial analogues in the spinning of polymeric fibres and in the shaping and blowing of glass sheets and shells. This second set of applications has provided a new impetus to the study of these problems using a combination of approaches.

At a theoretical level, a systematic asymptotic reduction of the full governing equations to the thin geometry of interest was carried out by Buckmaster, Nachman & Ting (1975), who investigated the large-amplitude deformation of a filament. Building on their scaling relations, Howell (1994, 1996) developed asymptotic equations governing the evolution of thin filaments and sheets in a variety of scenarios. In particular he derived equations for small deformations of viscous sheets equivalent to the Föppl–von Kármán equations for elastic plates – a linearized version thereof had been stated by analogy by Benjamin & Mullin (1988). Subsequently, a number of bending, stretching and buckling phenomena involving viscous filaments and planar deformations of viscous sheets have been explained: Yarin & Tchavdarov (1996) considered the onset of buckling in a filament impinging on a wall; Teichman & Mahadevan (2003) considered the viscous catenary using a combination of scaling, asymptotic and numerical approaches; Mahadevan, Ryu & Samuel (1998) and Skorobogatiy & Mahadevan (2000) provided a simple physical picture for the different regimes of coiling and folding of filaments on impact with a stationary surface; and Chiu-Webster & Lister (2006) considered the complex 'stitching' patterns of a filament impacting a moving surface. Somewhat fewer studies have investigated three-dimensional deformation of sheets: Silveira, Chaieb & Mahadevan (2000) considered the wrinkling of a ruptured viscous bubble collapsing under its own weight; Teichman (2002) considered the buckling of sheared viscous sheets in both a rectilinear and Couette geometry; Ribe (2001) derived asymptotic equations for sheets of high curvature and analysed aspects of geophysical problems such as trench rollback; Slim *et al.* (2009) briefly considered buckling of a thin viscous sheet by an underlying, less viscous fluid flow; and Mahadevan, Bendick & Liang (2010) analysed the form of tectonic subduction zones. This summary is by no means comprehensive but highlights the evolution of, and recent interest in, viscous buckling problems, especially involving two-dimensional deformation of a viscous plate or shell.

Here we study the shearing of a thin, very viscous sheet in a plane Couette geometry. Specifically, we consider an initially uniform, thin layer of viscous Newtonian fluid of finite width and infinite length sheared by the constant-velocity motion of bounding walls. The layer floats on a deep lower fluid, which contributes interfacial tension and a gravitational restoring force. The upper surface is open to the atmosphere and only experiences surface tension. Contrary to the situation for an infinitely thick sheet, which is linearly stable to shear for all values of the shear rate, the thin sheet can and does respond by buckling when sheared. We present the conditions for the onset of this linear instability, as well as growth rates and mode profiles above onset, expanding on the work of Teichman (2002).

The elastic counterpart to this problem was first studied by Southwell & Skan (1924) using the linearized Föppl–von Kármán equations. The behaviour at the onset of buckling has to some degree been verified experimentally, and the linear and

nonlinear behaviour above onset described using this model is also in reasonable agreement with experiments (see Balmforth, Craster & Slim 2008, and references therein). In contrast, there has been little previous work on the viscous problem, with the only detailed theoretical study due to Benjamin & Mullin (1988), who analysed a linear viscous plate model in a planar rectilinear geometry with a base state corresponding to simple shear. This led to a prediction that the onset of the instability arose at infinitesimal wavelengths relative to the plate width. Arguing that this is inconsistent, they present conditions for the onset of instability using an approximate short-wave, linear analysis of the full Stokes equations ignoring sidewall boundary conditions. On the experimental side, all studies have been in annular configurations (Taylor 1969; Suleiman & Munson 1981; Benjamin & Mullin 1988; Teichman 2002), a geometry that is fundamentally different from the rectangular one because the annular radius provides an additional length scale. In this case, the viscous plate model predicts the onset of buckling at moderate wavelength, in good agreement with experiments (see Teichman 2002).

Here we use both the full Stokes equations and the viscous plate model to investigate growth rates of infinitesimal perturbations to the simply sheared planar base state. Using the former, we show numerically that the thickest plate that can buckle has an aspect ratio of approximately 0.6 and is stabilized by internal viscous resistance alone. For thinner sheets with surface tension but no buoyancy, we establish the dependence of the critical wall speed on the plate width, thickness and surface tension coefficients. The viscous plate model is unable to reproduce these onset conditions except in the limit of vanishing plate thickness (where infinitesimal wavelengths are permissible). Nevertheless, for plates of aspect ratio up to around 0.04, given the system parameters at onset, the most unstable mode for this model accurately reproduces the mode profile and wavelength predicted using the full Stokes equations. Above onset, the most unstable mode has moderate wavelength, is stationary in the frame of the centreline, has crests and troughs aligned at approximately 45° to the sidewalls, and closely resembles the modes of the elastic analogue problem. Waves shorter than order the plate thickness are suppressed by internal viscous resistance. The shortest unstable modes form a pair of travelling waves, each concentrated in one half of the plate and propagating at a fraction of the corresponding wall speed. These modes cannot be captured by the asymptotic viscous plate model, which does not contain the advection term responsible for symmetry breaking. By modifying the model to include this term, we show that we can accurately recover the critical wavenumber and associated growth rates, propagation speeds and mode profiles.

In § 2 we describe the geometry and the relevant non-dimensional parameters. In § 3 we formulate the low-dimensional viscous plate model. Using this model in § 4, we briefly describe details of pure compression to set the scene for the shear instability, and present a parameter space investigation of the onset of shear-induced buckling, as well as the growth rates and mode profiles. In § 5, we turn to the full Stokes description. We present the linearized perturbation equations about the simple uniformly sheared base state, analyse its stability as a function of the problem parameters, and compare our results to those of the low-dimensional plate model, that model incorporating advection and the short-wavelength approximation due to Benjamin & Mullin (1988). In § 6 we summarize our results as a function of the parameter space, before presenting our conclusions in § 7.

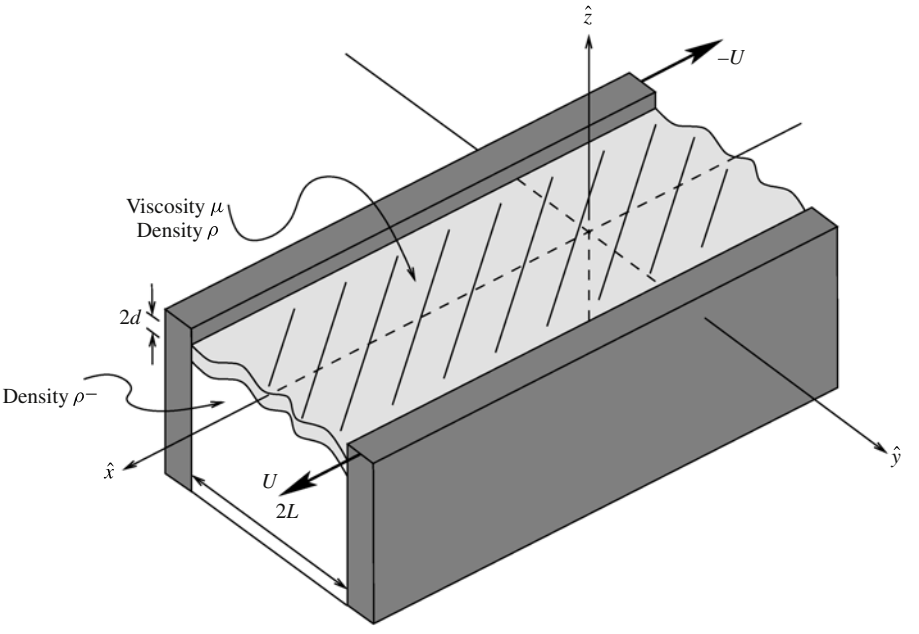

FIGURE 1. Viscous plate sheared by the motion of bounding walls.

2. Geometry

We start with a description of the geometry and the fundamental non-dimensional parameters. The configuration is sketched in figure 1: a thin layer ('plate') of very viscous, Newtonian, incompressible fluid of viscosity μ and density ρ floats on a deep layer of fluid with density $\rho^- > \rho$. We assume that inertia in the plate and viscosity in the underlying fluid are both negligible (Reynolds numbers in the plate are of the order 10^{-3} and viscosity ratios between the underlying fluid and the plate are of the order 10^{-5} in typical experiments). The upper surface is open to the atmosphere. The viscous plate has initially uniform thickness $2d$, width $2L$ and infinite length. We use Cartesian coordinates to describe the system, with the origin on the undeformed centreline, $\hat{x}$ axis directed along its length, $\hat{y}$ axis its width and $\hat{z}$ axis perpendicular to its undeformed centre-plane. Throughout, we shall use variables with hats to denote dimensional quantities and variables without hats to denote dimensionless ones. Along the lateral edges $\hat{y} = \pm L$, the plate is clamped to and sheared by the bounding walls, which move parallel to their length with velocity $\pm U$.

Three non-dimensional parameters naturally arise in the problem: the aspect ratio of the plate,

$$\alpha = d/L; \tag{2.1}$$

the scaled, inverse capillary numbers for the upper and lower surfaces and their mean,

$$\Gamma^{\pm} = \gamma^{\pm}/(\alpha\mu U), \quad \Gamma = (\Gamma^{+} + \Gamma^{-})/2, \tag{2.2}$$

where $\gamma^{\pm}$ are the coefficients of surface tension at the two surfaces; and the gravity numbers,

$$G = \rho g L^2/(\alpha\mu U), \quad G^{-} = \rho^{-} g L^2/(\alpha\mu U), \tag{2.3}$$

where g is gravity. These measure the importance of gravity on the plate and on the underlying fluid, respectively, relative to viscous shear in the plate. The appearance of the aspect ratio in the inverse capillary and gravity numbers ensures that the stabilizing effects of surface tension and gravity scale in the same way as the destabilizing effect of shear with variations in the plate thickness.

3. Low-dimensional viscous plate theory: formulation

The viscous plate equations are valid for small deflections of a very viscous fluid sheet whose thickness is much smaller than any extrinsic horizontal length scale such as the channel width or intrinsic length scale such as the wrinkle wavelength. For such sheets, out-of-plane sinuous deformations occur much quicker than varicose thickening and thinning (Howell 1996), and only the former are captured by the model. Thus the sheet thickness remains constant at $2d$, and the dynamics are best described in terms of the mid-plane displacement $\hat{H}$ from $\hat{z} = 0$. A physically motivated asymptotic derivation of the governing equations is given in appendix A; here we provide a summary.

Balance of forces in the plane of the sheet leads to (see (A 10))

$$\hat{\boldsymbol{\nabla}} \cdot \hat{\boldsymbol{\Sigma}} = \boldsymbol{0}, \tag{3.1}$$

where the gradient operator involves only the in-plane components $(\hat{x}, \hat{y})$ (this will be our convention throughout, unless explicitly stated otherwise). Here $\hat{\boldsymbol{\Sigma}}$ is the tensor of in-plane stresses acting on a cross-section of the sheet given by (see (A 8))

$$\hat{\boldsymbol{\Sigma}} = 4\mu d[\hat{\boldsymbol{E}} + \mathrm{tr}(\hat{\boldsymbol{E}})\boldsymbol{I}], \tag{3.2}$$

where $\boldsymbol{I}$ is the two-dimensional identity and $\hat{\boldsymbol{E}}$ is the in-plane deformation rate tensor given by (see (A 9))

$$\hat{\boldsymbol{E}} = \tfrac{1}{2}(\hat{\boldsymbol{\nabla}}\hat{\boldsymbol{u}}_h + \hat{\boldsymbol{\nabla}}\hat{\boldsymbol{u}}_h^{\mathrm{T}}) + \tfrac{1}{2}(\hat{\boldsymbol{\nabla}}\hat{H}\hat{\boldsymbol{\nabla}}\hat{w} + \hat{\boldsymbol{\nabla}}\hat{w}\hat{\boldsymbol{\nabla}}\hat{H}), \tag{3.3}$$

where superscript T denotes transpose, $\hat{\boldsymbol{u}}_h$ is the in-plane velocity field in the mid-surface of the plate and $\hat{w}$ is the out-of-plane velocity, given by

$$\hat{w} = \frac{\partial \hat{H}}{\partial \hat{t}}. \tag{3.4}$$

We note that the pressure appears indirectly in the expression (3.2) via a Trouton ratio (of 4 in two dimensions) and the trace of the deformation rate tensor. In (3.3), the first two terms are due to in-plane velocity gradients, while the last two describe the stretching rate of the mid-surface due to out-of-plane deformation and arise from differentiating the term $(\hat{\boldsymbol{\nabla}}\hat{H})^2$. Equation (3.4) couples the centre-plane deflection directly to the fluid velocity perpendicular to the sheet (see (A 7)).

The vertical force balance equation yields (see (A 12))

$$\tfrac{8}{3}\mu d^3\hat{\boldsymbol{\nabla}}^4\hat{w} = \hat{\boldsymbol{\nabla}} \cdot (\hat{\boldsymbol{\Sigma}} \cdot \hat{\boldsymbol{\nabla}}\hat{H}) + (\gamma^+ + \gamma^-)\hat{\boldsymbol{\nabla}}^2\hat{H} - \rho^- g\hat{H}. \tag{3.5}$$

Here the left-hand side is the Laplacian of the rate of change of mean curvature, describing the time-dependent viscous resistance to bending. In conjunction with (3.4), it can be shown that this term, whose effect is largest for short waves, regulates growth or decay rates of out-of-plane modes, but does not control whether the system is stable or unstable.

The first term on the right-hand side of (3.5) is the projection of the in-plane stresses in the out-of-plane direction; it is stabilizing if the principal in-plane stresses are tensile, and destabilizing if they are compressive. The second term on the right-hand side characterizes the role of surface tension and is stabilizing. It is useful to emphasize that both of these terms appear as Laplace pressures, coupling in-plane compression and tension with out-of-plane displacements, with the former potentially anisotropic and compressive, while the latter is always isotropic and tensile. Thus if in-plane flow-induced compressive stresses overwhelm surface tension at any wavelength, then they will do so for all wavelengths, and surface tension cannot provide a short-wavelength cutoff in this model. The final term on the right-hand side is a consequence of buoyancy and also plays a stabilizing role. Thus, while all terms on the right-hand side are active at all length scales, the first two are most prominent at short wavelengths while the last is most significant at long wavelengths.

We note that the model ignores contributions due to advection, an omission that has two significant implications. First, the model is not material-frame-invariant relative to translations and rotations in the plane. This is asymptotically correct in the limit $\alpha \to 0$, provided we use a frame of reference in which the advection of perturbations into a region is insignificant compared to the generation of perturbations by the out-of-plane velocity. Second, we shall see in § 5 that the advective terms are fundamental for describing certain qualitative features at moderately short wavelengths. Reincorporating the advective terms at leading order replaces the standard expression (3.4) with

$$\hat{w} = \frac{\partial \hat{H}}{\partial \hat{t}} + \hat{\bar{\boldsymbol{u}}}_h \cdot \hat{\boldsymbol{\nabla}} \hat{H}. \tag{3.6}$$

This eliminates the apparent inconsistency associated with frame indifference and extends the predictive power of the model. However, it requires the incorporation of higher-order terms into the leading-order model in a non-asymptotic fashion. In this section and § 4, we shall use (3.4); in subsequent sections we shall also present results using (3.6), and refer to that model as the advection-augmented plate.

Along the lateral boundaries

$$\hat{\bar{\boldsymbol{u}}}_h = (\pm U, 0), \quad \hat{w} = \partial \hat{w}/\partial \hat{y} = 0, \quad \text{on } \hat{y} = \pm L. \tag{3.7a,b,c}$$

3.1. *Scaled equations*

We scale using the sheet half-width L as a length and the wall speed U as a velocity, and include factors of the aspect ratio appropriate for a thin sheet (see appendix A) using hats to denote dimensional variables. Thus we set

$$\hat{\bar{\boldsymbol{u}}}_h = U \bar{\boldsymbol{u}}_h, \quad \hat{w} = (U/\alpha) w, \quad (\hat{x}, \hat{y}) = L(x, y), \quad \hat{H} = \alpha L H, \tag{3.8}$$

$$\hat{\boldsymbol{E}} = (U/L)\boldsymbol{E}, \quad \hat{\boldsymbol{\Sigma}} = \alpha \mu U \boldsymbol{\Sigma}, \quad \hat{t} = \alpha^2 (L/U) t, \tag{3.9}$$

reducing the system (3.1)–(3.5) and (3.7) to

$$\boldsymbol{\nabla} \cdot \boldsymbol{\Sigma} = \boldsymbol{0}, \quad \frac{8}{3}\nabla^4 w = \boldsymbol{\nabla} \cdot (\boldsymbol{\Sigma} \cdot \boldsymbol{\nabla} H) + 2\Gamma \nabla^2 H - G^{-} H, \quad \frac{\partial H}{\partial t} = w, \tag{3.10a,b,c}$$

$$\boldsymbol{\Sigma} = 4[\boldsymbol{E} + \mathrm{tr}(\boldsymbol{E})\boldsymbol{I}], \quad \boldsymbol{E} = \frac{1}{2}(\boldsymbol{\nabla} \bar{\boldsymbol{u}}_h + \boldsymbol{\nabla} \bar{\boldsymbol{u}}_h^{\mathrm{T}} + \boldsymbol{\nabla} H \boldsymbol{\nabla} w + \boldsymbol{\nabla} w \boldsymbol{\nabla} H), \tag{3.10d,e}$$

with boundary conditions

$$\bar{\boldsymbol{u}}_h = (\pm 1, 0), \quad w = \partial w/\partial y = 0 \quad \text{on } y = \pm 1, \tag{3.10f,g,h}$$

where the non-dimensional surface tension and buoyancy parameters Γ and G^- are as defined in § 2.

These governing equations for the dynamics of thin viscous sheets are similar to those for thin elastic sheets via the Stokes–Rayleigh analogy; we clarify the connection in appendix B.

4. Low-dimensional viscous plate theory: buckling analysis

We begin with a brief discussion of a viscous plate subject to pure compression (see Biot 1961; Ramberg 1963) to clarify the role of surface tension and gravity. In this case the bounding walls move perpendicular rather than parallel to their length, but the same governing framework applies.

4.1. *Pure compression*

The flat base state subject to compression is given by

$$\bar{\boldsymbol{u}}_{hb} = (0, -y), \quad H_b = w_b = 0, \tag{4.1}$$

with compressive in-plane stresses

$$\boldsymbol{\Sigma}_b = \begin{pmatrix} -4 & 0 \\ 0 & -8 \end{pmatrix}, \tag{4.2}$$

where subscript b denotes base. Onset of the instability can be gleaned from the evolution equations for the out-of-plane displacement (3.10*b*,*c*), which become

$$\frac{8}{3}\frac{\partial^5 H}{\partial y^4 \partial t} = -2(\Gamma - 4)\frac{\partial^2 H}{\partial y^2} - G^- H, \tag{4.3}$$

for infinitesimal perturbations. We look for short-wavelength solutions and thus ignore lateral boundary conditions and set $H(y, t) = \mathrm{e}^{\sigma t}\cos ky$. Then the growth rate σ is given by

$$\tfrac{8}{3}\sigma = 2(\Gamma - 4)/k^2 - G^-/k^4, \tag{4.4}$$

for wavenumber k. If $\Gamma > 4$, then perturbations of all wavenumbers decay. Conversely, if $\Gamma < 4$, then wavenumbers $k > \sqrt{G^-/2(4-\Gamma)}$ are unstable, with longer waves suppressed by buoyancy. The most unstable wavenumber is $k = \sqrt{G^-/(4-\Gamma)}$. Because onset is predicted to occur at infinitesimal wavelengths, the condition $\Gamma = 4$ may only be accurate for arbitrarily thin plates. However, for $G^-/(4-\Gamma)$ not too large, the model is more generally valid, and so the structure and wavelength of the most unstable mode should be captured correctly.

4.2. *Simple shear*

Shear is associated with motion parallel to the boundary and implies that we must now consider the evolution of infinitesimal perturbations to the flat base state,

$$\bar{\boldsymbol{u}}_{hb} = (y, 0), \quad H_b = w_b = 0, \tag{4.5a,b,c}$$

having in-plane stresses

$$\boldsymbol{\Sigma}_b = \begin{pmatrix} 0 & 2 \\ 2 & 0 \end{pmatrix}. \tag{4.5d}$$

Introducing normal mode perturbations $\delta\tilde{f}(y)\,\mathrm{e}^{\mathrm{i}kx+\sigma t}$ to each variable $f(x, y, t)$, where σ is the growth rate, k the wavenumber and $\delta \ll 1$ the amplitude, substituting into the governing equations (3.10) and linearizing about the base state, we obtain the eigenvalue problem

$$\frac{8}{3}\left(\frac{\partial^4}{\partial y^4} - 2k^2\frac{\partial^2}{\partial y^2} + k^4\right)\tilde{w} = 4\mathrm{i}k\frac{\partial \tilde{H}}{\partial y} + 2\Gamma\left(\frac{\partial^2 \tilde{H}}{\partial y^2} - k^2\tilde{H}\right) - G^{-}\tilde{H}, \quad \tilde{w} = \sigma\tilde{H}, \tag{4.6a,b}$$

subject to the boundary conditions $\tilde{H} = \partial\tilde{H}/\partial y = 0$ on $y = \pm 1$. To find σ for a given k, we discretize the above equation in y using a Chebyshev pseudo-spectral method (Trefethen 2000) and solve the resulting generalized eigenvalue problem using the `eig` routine of MATLAB.

It can be shown that (4.6) is self-adjoint (e.g. following an analysis similar to that of Southwell & Skan (1924) for the elastic problem), and thus $\sigma \in \mathbb{R}$ and all modes are stationary. However, as noted earlier, the viscous plate model does not preserve material frame invariance and modes would also appear stationary in reference frames fixed with either wall. Again, the reason is that in-plane advection of wrinkles contributes negligibly to the evolution of the centre-plane deflection compared to the out-of-plane velocity. Physically we expect that modes spanning the width of the plate cannot be biased by either bounding wall and thus are stationary in the frame of the centreline. This is captured by reintroducing advection at leading order and is shown to be correct in the full Stokes calculations described in § 5.

4.2.1. $G^{-} = \Gamma = 0$

The only stabilizing mechanisms in the viscous plate model are due to surface tension and buoyancy; without them the sheet buckles at any shear rate and all wavenumbers are unstable as shown in figure 2(*a*). Shear preferentially couples to the shortest wavelengths, but these waves are also most inhibited by the stabilizing influence of the dynamic bending resistance. Thus there is a most unstable mode at an intermediate wavelength, $\lambda = 2\pi/k = 3.32$. This mode spans the width of the plate and has crests and troughs aligned at roughly 45° (figure 2*b*), corresponding to the direction of principal compression for a simple shear flow. There is also a cascade of subdominant modes having smaller growth rates. These differ from the dominant mode by having multiple crests and troughs across the width of the plate, as shown in figure 2(*c*).

In contrast to a viscous plate, an elastic plate is stable to out-of-plane buckling when the shear is less than a finite threshold (Southwell & Skan 1924). However, given the Stokes–Rayleigh analogy, we expect there to be a close relationship between the instabilities in the two cases; in appendix B.1 we show that the structure and wavelength of the fastest growing viscous mode are identical to those of the elastic mode observed at onset.

4.2.2. $G^{-},\ \Gamma \neq 0$

As shown in figure 3, surface tension and buoyancy both stabilize long waves, but neither provides a short-wave cutoff. This somewhat counter-intuitive role of surface tension may be explained by noting that, in the viscous plate model, surface tension cannot provide a short-wave cutoff if it is exceeded by in-plane flow-induced compression. Conversely, since long waves are only weakly aligned with the direction of shear-induced compression, even the small effect of surface tension at such wavelengths is sufficient to suppress them.

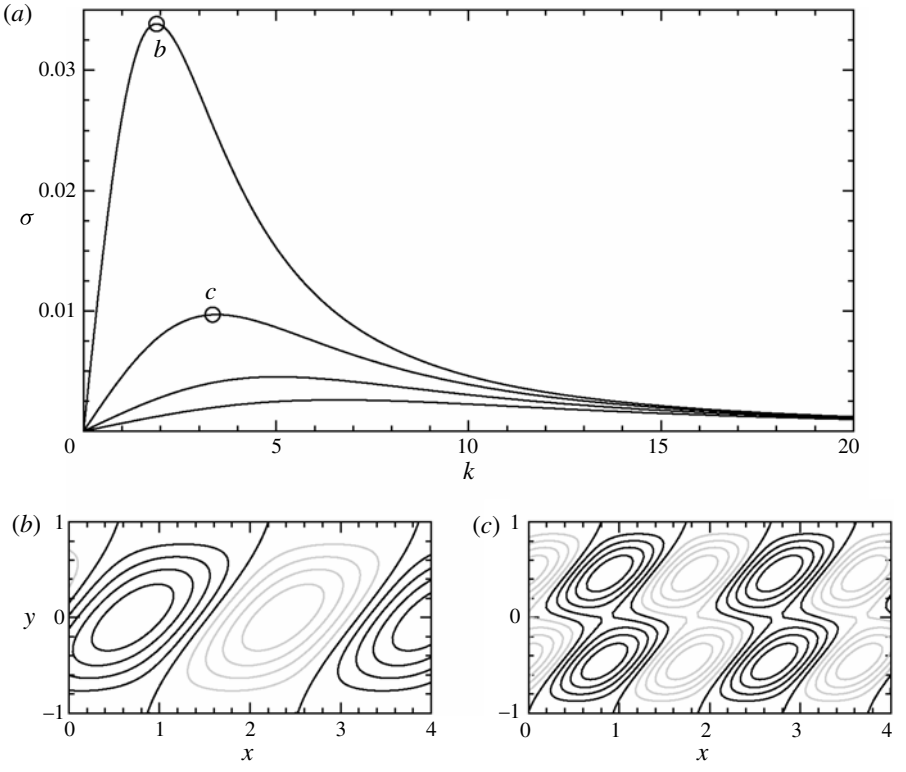

FIGURE 2. (*a*) Growth rates for the four most unstable modes for the viscous plate model (4.6) with $\Gamma = G^- = 0$. Contours of centre-plane displacements are shown in (*b*) and (*c*) for the two dominant modes' most unstable wavenumber. Grey/black curves indicate deflections of opposite sign. Perturbations are normalized to have a maximum amplitude of unity and contours are equally spaced at intervals of 0.2.

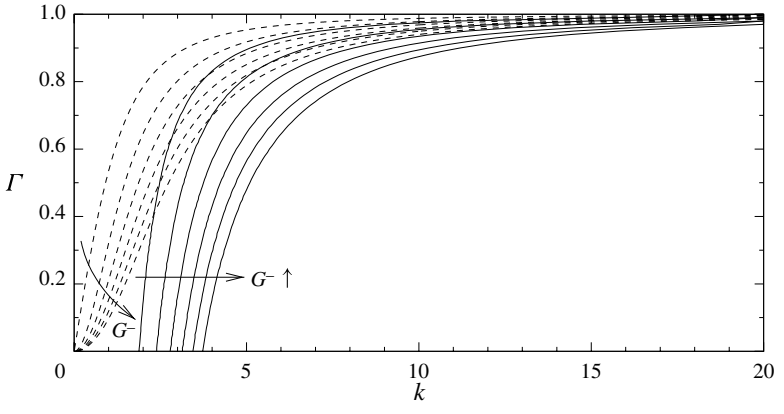

FIGURE 3. Most unstable wavenumber (solid curves) and smallest unstable wavenumber (dashed curves) for varying surface tension Γ for the plate model (4.6). Curves are shown for gravity numbers G^- increasing in the direction of the arrow from 0 to 5 in intervals of unity.

As Γ and G^- increase, the long-wave cutoff shifts to increasingly short waves and, in the limit $\Gamma \uparrow 1$, only the shortest waves remain unstable. As for pure compression, this is inaccurate for all but the thinnest plates because the viscous plate model is generally not applicable in the short-wave limit. However, above the onset of the buckling instability, the most unstable mode has moderate wavelength and thus should be faithfully reproduced.

5. Stokes formulation and buckling analysis

To find onset conditions for non-vanishingly thin sheets, to investigate the behaviour of short waves and to verify the predictions of the asymptotic viscous plate theory of the previous sections, we turn to a linear stability analysis for the full Stokes equations.

5.1. *Governing equations*

The equations for conservation of mass and momentum in an incompressible fluid are given by

$$\hat{\boldsymbol{\nabla}} \cdot \hat{\boldsymbol{u}} = 0, \quad \boldsymbol{0} = \hat{\boldsymbol{\nabla}} \cdot \hat{\boldsymbol{\sigma}} - \rho g \boldsymbol{e}_z, \tag{5.1a,b}$$

where the gradient operator is now three-dimensional, $\hat{\boldsymbol{u}} = (\hat{u}, \hat{v}, \hat{w})$ is the full three-dimensional velocity and $\hat{\boldsymbol{\sigma}}$ is the Cauchy stress given by

$$\hat{\boldsymbol{\sigma}} = -\hat{p}\boldsymbol{I} + \mu(\hat{\boldsymbol{\nabla}}\hat{\boldsymbol{u}} + \hat{\boldsymbol{\nabla}}\hat{\boldsymbol{u}}^{\mathrm{T}}), \tag{5.2}$$

where $\hat{p}$ is pressure, superscript T denotes transpose and the gradient operator is again three-dimensional.

On the solid bounding walls, we prescribe no-slip and no-penetration conditions,

$$\hat{\boldsymbol{u}} = (\pm U, 0, 0) \quad \text{on } \hat{y} = \pm L, \tag{5.3}$$

while on the free surfaces at $\hat{z} = \hat{\zeta}^{\pm}(\hat{x}, \hat{y}, \hat{t})$, we apply traction boundary conditions. On the upper surface, the plate is subject only to surface tension and

$$\hat{\boldsymbol{\sigma}} \cdot \boldsymbol{n}^+ = -\gamma^+ \hat{\kappa}^+ \boldsymbol{n}^+ \quad \text{on } \hat{z} = \hat{\zeta}^+, \tag{5.4}$$

with normal $\boldsymbol{n}^+ = (-\partial\hat{\zeta}^+/\partial\hat{x}, -\partial\hat{\zeta}^+/\partial\hat{y}, 1)$ and curvature $\hat{\kappa}^+ = \hat{\boldsymbol{\nabla}} \cdot \boldsymbol{n}^+$ (to simplify the presentation, we do not use unit surface normals; this is permissible because we only consider infinitesimal deformations). On the lower surface, the plate experiences a pressure from the underlying fluid in addition to surface tension, so that

$$\hat{\boldsymbol{\sigma}} \cdot \boldsymbol{n}^- = \gamma^- \hat{\kappa}^- \boldsymbol{n}^- - \hat{p}^- \boldsymbol{n}^- \quad \text{on } \hat{z} = \hat{\zeta}^-, \tag{5.5}$$

with variables defined as above. In the underlying fluid, we neglect inertial and viscous contributions. Thus the pressure is hydrostatic and follows the relation

$$-\hat{p}^- = -2\rho g d + \rho^- g(d + \hat{\zeta}^-). \tag{5.6}$$

We additionally have the kinematic conditions

$$\frac{\partial\hat{\zeta}^{\pm}}{\partial\hat{t}} + \hat{u}\frac{\partial\hat{\zeta}^{\pm}}{\partial\hat{x}} + \hat{v}\frac{\partial\hat{\zeta}^{\pm}}{\partial\hat{y}} = \hat{w} \quad \text{on } \hat{z} = \hat{\zeta}^{\pm}, \tag{5.7}$$

where $\hat{t}$ is time.

5.1.1. *Scaled equations*

To aid comparison with results from the low-dimensional viscous plate model, we scale the basic variables following (3.9) and appendix A (the appendix also gives a discussion of the choice of scalings), and thus set

$$\hat{\boldsymbol{u}} = U(u, v, w/\alpha), \quad \hat{\boldsymbol{x}} = L(x, y, \alpha z), \quad \hat{t} = (\alpha^2 L/U)t, \quad \hat{\zeta}^{\pm} = \alpha L \zeta^{\pm}, \quad \hat{p} = (\mu U/L)p, \tag{5.8}$$

$$(\hat{\sigma}_{xx}, \hat{\sigma}_{xy}, \hat{\sigma}_{yy}, \hat{\sigma}_{xz}, \hat{\sigma}_{yz}, \hat{\sigma}_{zz}) = (\mu U/L)(\sigma_{xx}, \sigma_{xy}, \sigma_{yy}, \alpha\sigma_{xz}, \alpha\sigma_{yz}, \alpha^2\sigma_{zz}). \tag{5.9}$$

The governing equations then become

$$0 = \frac{\partial u}{\partial x} + \frac{\partial v}{\partial y} + \frac{1}{\alpha^2}\frac{\partial w}{\partial z}, \tag{5.10a}$$

$$0 = \boldsymbol{\nabla} \cdot \boldsymbol{\sigma} - G\boldsymbol{e}_z, \tag{5.10b}$$

$$\boldsymbol{\sigma} = \begin{pmatrix} -p + 2\dfrac{\partial u}{\partial x} & \dfrac{\partial u}{\partial y} + \dfrac{\partial v}{\partial x} & \dfrac{1}{\alpha^2}\left(\dfrac{\partial u}{\partial z} + \dfrac{\partial w}{\partial x}\right) \\ \dfrac{\partial u}{\partial y} + \dfrac{\partial v}{\partial x} & -p + 2\dfrac{\partial v}{\partial y} & \dfrac{1}{\alpha^2}\left(\dfrac{\partial v}{\partial z} + \dfrac{\partial w}{\partial y}\right) \\ \dfrac{1}{\alpha^2}\left(\dfrac{\partial u}{\partial z} + \dfrac{\partial w}{\partial x}\right) & \dfrac{1}{\alpha^2}\left(\dfrac{\partial v}{\partial z} + \dfrac{\partial w}{\partial y}\right) & -\dfrac{1}{\alpha^2}p + 2\dfrac{1}{\alpha^4}\dfrac{\partial w}{\partial z} \end{pmatrix}, \tag{5.10c}$$

with free-surface boundary conditions

$$\boldsymbol{\sigma} \cdot \boldsymbol{n}^{+} = -\Gamma^{+}\kappa^{+}\check{\boldsymbol{n}}^{+} \quad \text{on } z = \zeta^{+}, \tag{5.10d}$$

$$\boldsymbol{\sigma} \cdot \boldsymbol{n}^{-} = \Gamma^{-}\kappa^{-}\check{\boldsymbol{n}}^{-} - [2G - (1 + \zeta^{-})G^{-}]\check{\boldsymbol{n}}^{-} \quad \text{on } z = \zeta^{-}, \tag{5.10e}$$

$$w = \frac{\partial \zeta^{\pm}}{\partial t} + \alpha^2\left(u\frac{\partial \zeta^{\pm}}{\partial x} + v\frac{\partial \zeta^{\pm}}{\partial y}\right) \quad \text{on } z = \zeta^{\pm}, \tag{5.10f}$$

and boundary conditions on the wall

$$\boldsymbol{u} = (\pm 1, 0, 0) \quad \text{on } y = \pm 1, \tag{5.10g}$$

where $\boldsymbol{n}^{\pm} = (-\partial\zeta^{\pm}/\partial x, -\partial\zeta^{\pm}/\partial y, 1)$, $\check{\boldsymbol{n}}^{\pm} = (-\alpha^2\partial\zeta^{\pm}/\partial x, -\alpha^2\partial\zeta^{\pm}/\partial y, 1)$, $\kappa^{\pm} = -\nabla^2\zeta^{\pm}$ and the parameters are as defined in § 2.

5.2. *Base state and perturbation equations*

We again assume a flat base state with a unidirectional, steady velocity profile and hydrostatic pressure:

$$\zeta_b^{\pm} = \pm 1, \quad \boldsymbol{u}_b = (y, 0, 0), \quad -p_b = \alpha^2 G(z - 1). \tag{5.11}$$

To consider the evolution of infinitesimal perturbations to this base state, we assume a normal mode decomposition, with each dependent variable $f(x, y, z, t)$ perturbed by an amount $\delta\tilde{f}(y, z)\,\mathrm{e}^{\mathrm{i}kx+\sigma t}$, where k is a wavenumber, σ the growth rate and $\delta \ll 1$ the amplitude. Making the appropriate substitutions into the governing equations (5.10) and linearizing about the base state, we obtain the eigenvalue problem for σ:

$$\mathrm{i}k\tilde{u} + \frac{\partial \tilde{v}}{\partial y} + \frac{1}{\alpha^2}\frac{\partial \tilde{w}}{\partial z} = 0, \quad -\mathrm{i}k\tilde{p} + \mathscr{L}\tilde{u} = -\frac{\partial \tilde{p}}{\partial y} + \mathscr{L}\tilde{v} = -\frac{\partial \tilde{p}}{\partial z} + \mathscr{L}\tilde{w} = 0, \tag{5.12a–d}$$

where $\mathscr{L} = -k^2 + \partial^2/\partial y^2 + (1/\alpha^2)\partial^2/\partial z^2$, subject to

$$\frac{\partial \tilde{u}}{\partial z} + \mathrm{i}k\tilde{w} = \alpha^2 \frac{\partial \tilde{\zeta}^{\pm}}{\partial y} \quad \text{on } z = \pm 1, \tag{5.12e}$$

$$\frac{\partial \tilde{v}}{\partial z} + \frac{\partial \tilde{w}}{\partial y} = \alpha^2 \mathrm{i}k\tilde{\zeta}^{\pm} \quad \text{on } z = \pm 1, \tag{5.12f}$$

$$-\frac{1}{\alpha^2}\tilde{p} + 2\frac{1}{\alpha^4}\frac{\partial \tilde{w}}{\partial z} = \Gamma^{+}\left(-k^2 + \frac{\partial^2}{\partial y^2}\right)\tilde{\zeta}^{+} - G\tilde{\zeta}^{+} \quad \text{on } z = 1, \tag{5.12g}$$

$$-\frac{1}{\alpha^2}\tilde{p} + 2\frac{1}{\alpha^4}\frac{\partial \tilde{w}}{\partial z} = -\Gamma^{-}\left(-k^2 + \frac{\partial^2}{\partial y^2}\right)\tilde{\zeta}^{-} + (G^{-} - G)\tilde{\zeta}^{-} \quad \text{on } z = -1, \tag{5.12h}$$

$$\sigma\tilde{\zeta}^{\pm} + \alpha^2 \mathrm{i}ky\tilde{\zeta}^{\pm} = \tilde{w}, \quad \text{on } z = \pm 1, \tag{5.12i}$$

and

$$\tilde{u} = \tilde{v} = \tilde{w} = \tilde{\zeta}^{\pm} = 0 \quad \text{on } y = \pm 1. \tag{5.12j–m}$$

We note that as $\alpha \to 0$ this system at leading order is identical to the eigenvalue problem (4.6) for the low-dimensional viscous plate theory. In other words, the perturbation expansion and the asymptotic analysis commute. This can be shown most readily by starting with the system above in a stress formulation and following an equivalent asymptotic analysis to that given in appendix A.

5.2.1. *Numerical method and spectrum*

We find the eigenvalues and eigenmodes of the system (5.12) numerically, using a Chebyshev pseudo-spectral discretization in y and z and solving the resulting generalized linear eigenvalue problem using the `eig` routine of MATLAB (Trefethen 2000). Since the pressure and velocity are collocated on the same grid points, to have sufficient equations we augment the boundary conditions on the free surfaces using the continuity equation, and the boundary conditions on the walls using the normal component of the momentum equation (cf. Gresho 1991; Canuto, Hussaini & Quarteroni 2007). We treat the corners as part of the walls (see appendix C for a discussion of these choices and convergence of the algorithm).

A sample spectrum for a particular set of parameters is shown in figure 4. It consists of both a discrete part (indicated by diamonds) and a continuous part (indicated by circles), as expected for shear instabilities (Schmid & Henningson 2001). The discrete part is further broken up into purely real eigenvalues and complex-conjugate pairs. The former correspond to stationary, sheet-spanning modes; example displacement profiles are shown in figure 5(*c*,*d*,i–iii). The latter correspond to a pair of travelling modes symmetric to one another under a 180° rotation about the vertical axis; example displacement profiles are shown in figure 5(*c*,*d*,iv,v). The continuous part of the spectrum corresponds to perturbations localized at a given cross-stream location y and travelling at the local base-state velocity. These modes are stable (although, for weak stabilization, only just so). A 'balloon' of incompletely resolved modes surrounds this continuous spectrum (progressively collapsing onto it with increasing resolution) and causes some numerical difficulties finding cutoffs where the continuous spectrum is just stable.

All solutions are presented for 28 grid points in y and 14 points in z (unless otherwise stated). We calculated all eigenvalues and mode structures at this resolution and verified them by comparison with their counterparts at a resolution of 40×20.

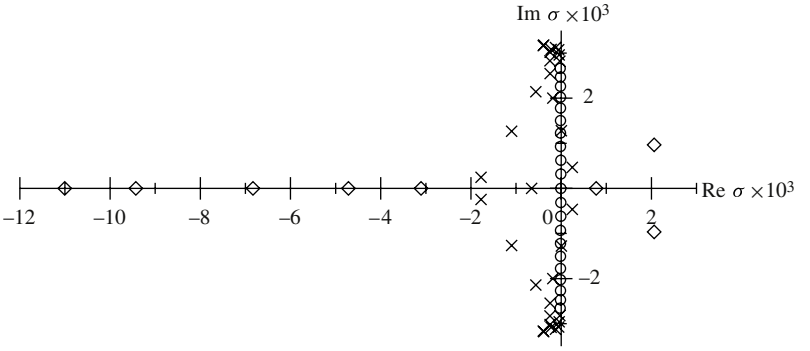

FIGURE 4. Eigenvalue spectrum for the Stokes equations (5.12) with $k = 8$, $\alpha = 0.02$, $\Gamma^+ = \Gamma^- = 0.5$ and $G = G^- = 0$. Diamonds are resolved modes in the discrete spectrum, circles are modes in the continuous spectrum and crosses are incompletely resolved modes (they still move perceptibly with increasing resolution). Resolution: 32 grid points in y and 16 in z.

5.3. *Dispersion relations*

To make the investigation of parameter space more manageable, we present results for plates stabilized only by an equal surface tension on the upper and lower surfaces, setting $G = G^- = 0$ and $\Gamma^+ = \Gamma^-$. Representative dispersion relations for the four most unstable modes are shown in figure 5, together with selected mid-plane displacement profiles. The structure of the dispersion relation is generally similar to the viscous plate prediction: shear couples most strongly to the shortest waves, but such modes are also most damped by viscous resistance, and thus the system is most unstable at intermediate wavenumber. Both long-wave and short-wave cutoffs exist. The longest waves are stabilized by surface tension, while the shortest are stabilized by an internal viscous resistance induced by shear deformations through the thickness. This is not accounted for in the low-dimensional plate model, which only has extensional deformations through the thickness.

For small and moderate wavenumbers, the four most unstable modes are stationary ($\mathrm{Im}\,\sigma = 0$ in figure 5*a*). However, at a critical wavenumber $k_{crit} \approx 7.5$, the two most unstable modes have equal growth rates, and for larger k they form a pair of travelling modes with complex conjugate growth rates. At a larger wavenumber still, the third and fourth modes undergo a similar bifurcation. The evolution of the mode structures with k reflects this changing behaviour: for small and moderate wavenumbers, the dominant mode has a single crest or trough that spans the width of the sheet and is aligned at approximately 45° (figure 5*c*,i–iii). The first sub-dominant mode initially has two extrema across the sheet with a weakly deformed centreline (figure 5*d*,i,ii). As k increases, the mid-surface deformation also increases, and eventually the mode consists of a single, somewhat sinuous crest or trough spanning the sheet (figure 5*d*,iii). At k_{crit}, the first two modes become identical, and when $k > k_{crit}$, they are related to one another by a 180° rotation about the z axis (figure 5*c*,*d*,iv,v). With increasing k, they become increasingly concentrated on one side of the plate and travel with a fraction of the corresponding wall speed (figure 5*a*).

We see that, for small and moderate wavenumbers, the viscous plate model approximates the growth rate and mode structures of the full Stokes equations very well (thick grey curves in figure 5*b*, and final pair of rows of profiles, figures 5*g*,*h*).

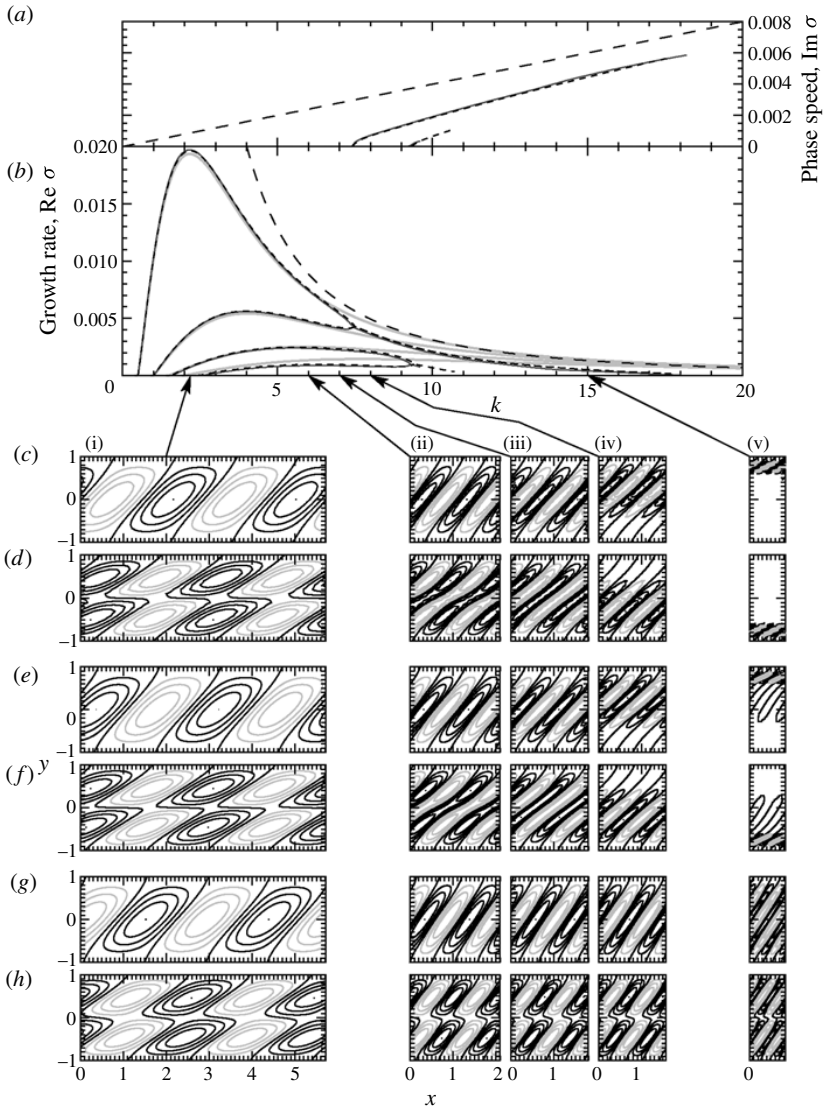

FIGURE 5. Perturbation properties for capillary numbers $\Gamma^+ = \Gamma^- = 0.3$, gravity numbers $G = G^- = 0$ and aspect ratio $\alpha = 0.02$. (*a*) Phase speed and (*b*) growth rate for the four most unstable modes: black solid curves are the full numerical solutions of the Stokes equations (5.12); thick grey curves are the viscous plate prediction; black short-dashed curves are the advection-augmented plate model; and black long-dashed curves are the maximum possible growth rates and phase speeds using the short-wave approximation. Curves are truncated where they become unreliable. Note that the phase speed is zero for the Stokes and augmented plate models for wavenumbers less than a critical value and for the viscous plate model for all wavenumbers. (*c–h*) Out-of-plane displacement contours at the indicated wavenumbers: (*c*,*d*) full solutions, (*e*,*f*) advection-augmented plate and (*g*,*h*) viscous plate; (*c*,*e*,*g*) dominant mode and (*d*,*f*,*h*) next most unstable. Note that for the Stokes and augmented plate models, above the critical wavenumber these two modes have equal growth rate and are related to one another by a 180° rotation. Grey/black curves indicate deflections of opposite sign. Perturbations are normalized to have maximum amplitude of unity and contours are equally spaced in intervals of 0.25 (the 0 contour is omitted for $|y| > 0.6$ in (*c*,*d*,v)).

However, the transition from stationary to travelling waves at k_{crit} is not captured, and indeed cannot be captured by a regular asymptotic expansion of any order in α.

To capture this transition requires a reintroduction of advection in the low-dimensional viscous plate theory. We do this by replacing (4.6*b*) with the full kinematic condition from (3.6), which in the dimensionless, spectral setting reads

$$\tilde{w} = \sigma \tilde{H} + \alpha^2 \mathrm{i}ky\tilde{H}. \tag{5.13}$$

Predictions using this modification are included in figure 5 with short-dashed curves and form the central pair of rows of profiles. They provide an accurate approximation of the behaviour at and around the critical wavenumber as well as improving the approximation at smaller k. Unfortunately, this modified model also does not appear to have a short-wave cutoff. However, the spectrum has a neutrally stable continuous part, and so it is difficult to state this definitively.

Just as the low-dimensional plate theory allows us to describe moderate- to long-wavelength deformations (relative to the thickness), one can ask if there is another asymptotic approximation that allows us to consider short-wave behaviour (relative to the thickness). The analysis of Benjamin & Mullin (1988) provides such a route and is summarized in appendix D. However, the predictions provide only a fair approximation to the short-wave behaviour (see figure 5*b*); the discrepancy is presumably because the dominant mode begins to concentrate near the outer walls and so lateral boundary conditions remain important.

5.4. *Comparing the Stokes and asymptotic theories: dependence on aspect ratio* α

To understand how well/poorly the low-dimensional viscous plate theory does in describing the buckling instability, we show a comparison of growth rates for the dominant mode at various aspect ratios in figure 6. The growth rates of the longest and most unstable wavelengths remain identical for aspect ratios up to 0.04 and are well described by the plate model (grey curve). The advection-augmented plate model (dashed curves) somewhat over-predicts the maximum growth rates for $\alpha \geqslant 0.04$, but accurately predicts k_{crit} and improves the estimate of the most unstable wavenumber. We can estimate how k_{crit} scales with α by balancing the bending-resistance-modulated advection term of order $k^5\alpha^2$ in the advection-augmented model with the shear term of order k. The resulting prediction $k_{crit}^2 = O(1/\alpha)$ is in good agreement with numerical solutions (inset of figure 6). Physically this results from progressively thinner plates buckling quicker, and thus only advection of increasingly short waves influencing mode structure. Short waves are cut off for $k_{cut} = O(1/\alpha)$, when wavelengths approach the plate thickness (inset of figure 6).

6. Stability diagrams for the onset of shear-induced buckling

With the analysis of the different regimes at hand, we can now present the stability diagrams for the buckling instability of a sheared plate in terms of the dimensionless parameters that characterize the forcing: the scaled surface tension relative to shear rate Γ and the geometrical aspect ratio α. Figure 7 shows the principal features of the instability for different Γ and α. Instability is possible for sheets of surprisingly large aspect ratio, up to $\sim$0.6 (figure 7*c*). In general, the long-wave cutoff and most unstable wavelength are well approximated by the low-dimensional plate model, even for reasonably thick plates, and the transition to travelling waves is captured by the advection-augmented version of the model. The short-wave cutoff is not well described by any of the approximations and appears to require full numerical

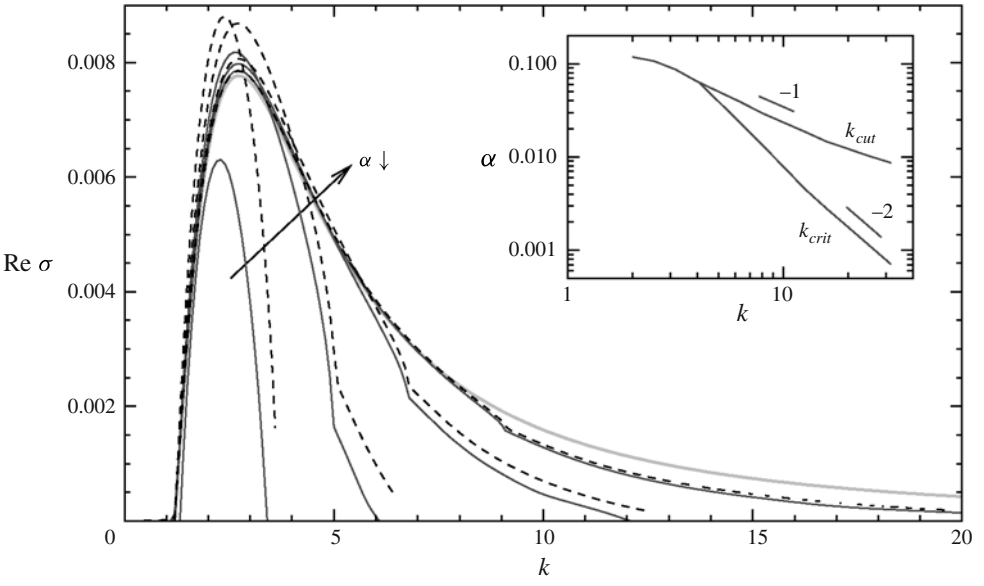

FIGURE 6. Growth rates for various aspect ratios $\alpha = 0.08, 0.05, 0.04, 0.02$ and 0.01 (in direction of arrow) for $\Gamma^+ = \Gamma^- = 0.6$, $G = G^- = 0$. Black solid curves are the full numerical solutions of the Stokes equations (5.12), the thick grey curve is the viscous plate prediction and black dashed curves are the advection-augmented plate model. Inset shows the critical wavenumber k_{crit} and short-wave cutoff as functions of the aspect ratio.

calculation. However, portions of the short-wave cutoff cannot be adequately resolved even with the full numerics once the most unstable mode becomes localized to the outer wall. Most likely, the reason is that very short waves for thin plates require very high resolution to resolve both the apparent pressure singularity at the walls (see appendix C) and the wave itself. This is particularly true when the continuous spectrum is just stable (Γ small or zero), but we do not pursue this aspect further.

7. Discussion and conclusions

We have presented conditions for the linear, shear-induced buckling of a viscous plate stabilized by internal viscous resistance, surface tension and buoyancy. In the limit of a vanishingly thin plate, a low-dimensional asymptotic theory of the dynamics yields the result that the onset of instability occurs at a scaled inverse shear rate $\Gamma = 1$ independent of buoyancy. For plates with a finite thickness stabilized only by an equal surface tension at the upper and lower surfaces, our numerical solutions of the eigenvalue problem based on the Stokes equations show that the most unstable mode has moderate wavelength: shear couples primarily to the shortest waves, but these are also most strongly suppressed by viscous resistance to bending and surface tension. This mode is stationary in the frame of the centreline of the plate, spans the width of the plate, has crests aligned at approximately 45° and is closely related to elastic shear modes that have been well known for more than 85 years.

We have compared results using the full Stokes equations and its two limiting theories, the long-wavelength viscous plate model and the short-wave approximation of Benjamin & Mullin (1988). The plate model predicts onset at $\Gamma = 1$ with infinitesimal wavelengths, which is only consistent and accurate for arbitrarily thin plates. However,

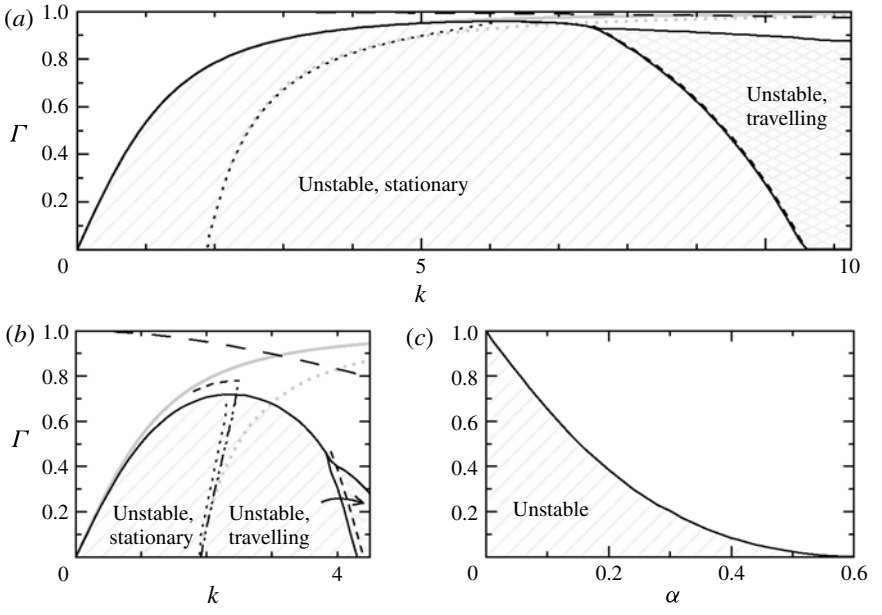

FIGURE 7. Instability region for the Stokes equations (5.12) (bounded by solid black curves) as functions of Γ for (*a*) $\alpha = 0.01$ and (*b*) 0.08 with $G = G^- = 0$ and $\Gamma^+ = \Gamma^-$. Unstable stationary and travelling modes are distinguished by labelling and are separated by a solid black curve indicating the critical wavenumber. The most unstable wavenumber is shown by a dotted black curve. Thick grey curves give the corresponding viscous plate predictions, black short-dashed curves are the advection-augmented plate model and black long-dashed are the short-wave approximation for the short-wave cutoff. In (*a*), the advection-augmented plate predictions for the long-wave cutoff and most unstable wavenumber are indistinguishable from the viscous plate predictions. The viscous plate model is unable to predict the transition to travelling waves; neither plate description can capture the short-wave cutoff. (*c*) Maximum Γ for instability as a function of α.

for plates up to $\alpha \approx 0.04$, given onset parameter values, the model accurately reproduces both the modal structure and the most unstable mode above onset. The short-wave model is somewhat inaccurate for both onset ($\Gamma = 1$ independent of α at an inconsistent, infinite wavelength) and growth rates, at least in the absence of buoyancy.

Thus we see that the viscous plate model is quite useful, even outside its range of validity. However, it has two shortcomings. The first is that it is not material-frame-invariant. This can be remedied by including advection at leading order, a modification that also extends the model's predictive power to reliably capture travelling waves that appear at moderately short wavelengths, even if this is not strictly correct in an asymptotic setting. The second shortcoming is that amplitude-saturated modes cannot be described because the equations become linear when the flow is steady, and thus the amplitude is indeterminate. This suggests that saturated modes have larger amplitude than assumed in the derivation of the governing equations, and moderate or large curvature descriptions (Howell 1994, 1996; Ribe 2001) may be necessary to describe their structure.

Perhaps surprisingly, there are no experiments in this rectangular Couette geometry, even though it is similar to many industrial flow settings associated with the float-

glass and polymer manufacturing industries. As alluded to in the introduction, the annular geometry has been studied but that problem is fundamentally different owing to the presence of an additional length scale. A few of the experiments by Suleiman & Munson (1981) do approach the rectangular limit and the observed modes are qualitatively consistent with our theory: they fill the width of the annulus, are stationary with respect to the centreline of the sheet, aligned at 45° to the bounding walls, and closely resemble elastic modes. Unfortunately, there are no reported data for the parameter values associated with the onset of the instability, so that the next step is clearly an experimental study of the onset of buckling in a long, rectangular Couette geometry.

Acknowledgement

L.M. acknowledges the Harvard NSF MRSEC center and the MacArthur Foundation.

Appendix A. Long-wavelength approximation for a viscous plate

Several derivations exist of the viscous plate model, from the analogy with the elastic plate by Benjamin & Mullin (1988) to the formal asymptotic expansion of Howell (1994, 1996). Our attempt is to provide more physical motivation for Howell's asymptotic derivation.

To avoid repetition, we begin with the governing Stokes equations given in (5.1)–(5.7) and non-dimensionalize them according to (5.8)–(5.9). We justify the scalings inherent in (5.8)–(5.9) for the limit of the aspect ratio $\alpha \to 0$ as follows. First, in-plane stresses $\hat{\boldsymbol{\sigma}}_h$ (where subscript h denotes in-plane components $\hat{x}$ and $\hat{y}$) are driven by boundary motions and scale as $\mu U/L$. Then, for small deflections of the plate of order α, these in-plane stresses generate out-of-plane stresses on a cross-section $\hat{\sigma}_{xz}$ and $\hat{\sigma}_{yz}$ of order $\alpha\mu U/L$ courtesy of the in-plane components of the force balance equations and the traction conditions. These components in turn generate an out-of-plane stress on the surface $\hat{\sigma}_{zz}$ of order $\alpha^2\mu U/L$ courtesy of the out-of-plane component of the force balance equations and the traction. Second, there must be internal viscous resistance to deformation; specifically, elongation on outer surfaces of wrinkles is resisted, as is compression on inner surfaces, thus $\partial\hat{u}/\partial\hat{z} \sim \partial\hat{w}/\partial\hat{x}$ and $\partial\hat{v}/\partial\hat{z} \sim \partial\hat{w}/\partial\hat{y}$ in the shear stresses $\hat{\sigma}_{xz}$ and $\hat{\sigma}_{yz}$. In consequence, the out-of-plane velocity $\hat{w}$ appears of order $1/\alpha$ larger than the in-plane, reflecting the fact that out-of-plane deformation is much easier than in-plane for a thin geometry. Thus we again arrive at the non-dimensional equations (5.10). (We note that these scalings are for the most general scenario for a fluid layer of aspect ratio $\alpha \ll 1$ that is almost flat. For the particular shear base state considered in this paper, the pressure in fact scales as $\alpha^2\mu U/L$ rather than $\mu U/L$. The pressure perturbation scales as $\mu U/L\delta$, where δ is the perturbation amplitude, rather than $\alpha^2\mu U/L\delta$.)

We now proceed to a regular asymptotic analysis, expanding each variable f as $f_0 + \alpha^2 f_2 + O(\alpha^4)$, substituting these into the governing equations and equating terms at each order in α.

For the scalings to be adhered to in the continuity equation (5.10*a*) and the expression in (5.10*c*) for σ_{zz}, we immediately find that the out-of-plane velocity is uniform across the plate

$$\frac{\partial w_0}{\partial z} = 0. \tag{A 1}$$

From the same two expressions at next order, we also obtain $\partial u_0/\partial x + \partial v_0/\partial y + \partial w_2/\partial z = 0$ and $-p_0 + 2\partial w_2/\partial z = 0$. Combining, these imply

$$-p_0 = 2\left(\frac{\partial u_0}{\partial x} + \frac{\partial v_0}{\partial y}\right). \tag{A 2}$$

Then at leading order the in-plane stresses σ_{xx}, σ_{xy} and σ_{yy} in (5.10*c*) become

$$\boldsymbol{\sigma}_{h0} = 2[\boldsymbol{e} + \mathrm{tr}(\boldsymbol{e})\boldsymbol{I}], \tag{A 3}$$

with $\boldsymbol{e} = (\nabla \boldsymbol{u}_{h0} + \nabla \boldsymbol{u}_{h0}^{\mathrm{T}})/2$, the in-plane part of the strain rate. The expressions for stresses σ_{xz} and σ_{yz} imply $\partial u_0/\partial z + \partial w_0/\partial x = 0$ and $\partial v_0/\partial z + \partial w_0/\partial y = 0$, respectively, from which we infer

$$\boldsymbol{u}_{h0} = -z\nabla w_0 + \bar{\boldsymbol{u}}_h(x, y), \tag{A 4}$$

where $\bar{\boldsymbol{u}}_h$ is the velocity on the centre-plane. The kinematic conditions (5.10*f*) on the free surfaces furnish

$$\frac{\partial \zeta_0^+}{\partial t} = \frac{\partial \zeta_0^-}{\partial t} = w_0. \tag{A 5}$$

Thus the plate retains uniform thickness

$$\zeta_0^+ - \zeta_0^- = 2 \tag{A 6}$$

and

$$\frac{\partial H_0}{\partial t} = w_0, \tag{A 7}$$

where $H_0 = (\zeta_0^+ + \zeta_0^-)/2$.

Now evaluating forces on a cross-section, we find

$$\boldsymbol{\Sigma} = \int_{\zeta_0^-}^{\zeta_0^+} \boldsymbol{\sigma}_{h0}\,\mathrm{d}z = 4[\boldsymbol{E} + \mathrm{tr}(\boldsymbol{E})\boldsymbol{I}], \tag{A 8}$$

with

$$\boldsymbol{E} = \tfrac{1}{2}(\nabla \boldsymbol{u}_h + \nabla \boldsymbol{u}_h^{\mathrm{T}} + \nabla H \nabla w + \nabla w \nabla H), \tag{A 9}$$

the in-plane deformation rate averaged across the thickness of the plate. Integrating the in-plane momentum equations (the x and y components of (5.10*b*)) across the cross-section and applying the traction conditions (the x and y components of (5.10*d*) and (5.10*e*)), we obtain the in-plane balance of forces

$$\nabla \cdot \boldsymbol{\Sigma} = \boldsymbol{0}. \tag{A 10}$$

Similarly evaluating moments, we find

$$\boldsymbol{M} = \int_{\zeta_0^-}^{\zeta_0^+} z\boldsymbol{\sigma}_{h0}\,\mathrm{d}z = -\frac{4}{3}[\nabla\nabla w_0 + \mathrm{tr}(\nabla\nabla w_0)\boldsymbol{I}] + H_0\boldsymbol{\Sigma}. \tag{A 11}$$

Integrating the out-of-plane momentum equation (the z component of (5.10*b*)) by parts across the cross-section and applying boundary conditions (the z components of (5.10*d*) and (5.10*e*)), we obtain the out-of-plane evolution equation

$$\nabla\nabla : \boldsymbol{M} + 2\Gamma\nabla^2 H_0 - G^- H_0 = 0, \tag{A 12}$$

where the term $\nabla\nabla : \boldsymbol{M}$ expands to $-(8/3)\nabla^4 w_0 + \nabla \cdot (\boldsymbol{\Sigma} \cdot \nabla H_0)$.

The system (A 7)–(A 12) provides the non-dimensional viscous plate equations (3.10*a*,*b*,*c*). The lateral boundary conditions are obtained on setting the velocity at bounding walls to the prescribed value; thus $\bar{u}_{h0}$ and w_0 take prescribed values and the normal component of $\boldsymbol{\nabla} w_0$ vanishes.

With some algebra, the next-order correction to the governing equations can be readily derived, although the boundary conditions at the walls become more complex. In particular, the next-order velocity components become higher-order polynomials in z across the plate thickness, so that, for example,

$$w_2(x, y, z) = \bar{w}_2(x, y) + \tfrac{1}{2} z^2 \nabla^2 w_0. \tag{A 13}$$

Thus directly imposing no slip at $y = \pm 1$ would imply an additional, and over-specifying, condition on w_0. This suggests that there is a boundary layer at the two walls, of thickness comparable to the thickness of the plate. We do not pursue this further, but note that similar boundary layers exist for elastic plates (e.g. Friedrichs & Dressler 1961).

Appendix B. Elastic versus viscous plate models

Consistent with the Stokes–Rayleigh analogy (Rayleigh 1945), there is a close connection between the governing equations for elastic and viscous plates as well as between the associated buckling instabilities. For an incompressible elastic material with Young's modulus Y, the governing Föppl–von Kármán equations are given by (e.g. Timoshenko & Woinowsky-Krieger 1959)

$$\hat{\boldsymbol{\nabla}} \cdot \hat{\boldsymbol{\Sigma}} = \boldsymbol{0}, \quad \tfrac{8}{9} Y d^3 \hat{\boldsymbol{\nabla}}^4 \hat{H} = \hat{\boldsymbol{\nabla}} \cdot (\hat{\boldsymbol{\Sigma}} \cdot \hat{\boldsymbol{\nabla}} \hat{H}) + T_0 \hat{\boldsymbol{\nabla}}^2 \hat{H} - \rho^- g \hat{H}, \tag{B 1}$$

$$\hat{\boldsymbol{\Sigma}} = \tfrac{4}{3} dY [\hat{\boldsymbol{E}} + \mathrm{tr}(\hat{\boldsymbol{E}}) \boldsymbol{I}], \quad \hat{\boldsymbol{E}} = \tfrac{1}{2} (\hat{\boldsymbol{\nabla}} \hat{\boldsymbol{u}}_h + \hat{\boldsymbol{\nabla}} \hat{\boldsymbol{u}}_h^{\mathrm{T}} + \hat{\boldsymbol{\nabla}} \hat{H} \hat{\boldsymbol{\nabla}} \hat{H}), \tag{B 2}$$

where we associate $\hat{\boldsymbol{E}}$ with the in-plane deformation tensor and $\hat{\hat{\boldsymbol{u}}}_h$ with the in-plane displacement of the centre-plane. To complete the analogy with the viscous plate, we have included T_0, an isotropic background tension ($T_0 > 0$) or compression ($T_0 < 0$), and a buoyant restoring force. This system becomes identical to the viscous plate model on identifying $\mu \partial / \partial \hat{t}$ with $Y/3$ and T_0 with $\gamma^+ + \gamma^-$. Boundary conditions (3.7) translate into clamped edges,

$$\hat{\hat{\boldsymbol{u}}}_h = (\pm U, 0), \quad \hat{H} = \partial \hat{H} / \partial \hat{y} = 0 \quad \text{on } \hat{y} = \pm L. \tag{B 3}$$

Scaling these equations according to (3.9) with $\mu \partial / \partial \hat{t}$ replaced by $Y/3$, we arrive at

$$\boldsymbol{\nabla} \cdot \boldsymbol{\Sigma} = \boldsymbol{0}, \quad \frac{8}{3} \frac{1}{\mathscr{S}} \nabla^4 H = \boldsymbol{\nabla} \cdot (\boldsymbol{\Sigma} \cdot \boldsymbol{\nabla} H) + 2\Gamma \nabla^2 H - G^- H, \tag{B 4}$$

$$\boldsymbol{\Sigma} = 4 [\boldsymbol{E} + \mathrm{tr}(\boldsymbol{E}) \boldsymbol{I}], \quad \boldsymbol{E} = \frac{1}{2} \left(\boldsymbol{\nabla} \bar{\boldsymbol{u}}_h + \boldsymbol{\nabla} \bar{\boldsymbol{u}}_h^{\mathrm{T}} + \frac{2}{\mathscr{S}} \boldsymbol{\nabla} H \boldsymbol{\nabla} H \right), \tag{B 5}$$

where $\mathscr{S} = U/(\alpha^2 L)$ is the dimensionless applied shear strain. Comparing these equations with those in § 3 makes the analogy between the elastic and viscous plate descriptions transparent.

B.1. *Shear instability*

It is useful to compare the buckling of a sheared viscous plate as described in § 4.2 with the classical calculation by Southwell & Skan (1924) for the buckling of a sheared elastic plate. The flat base state for an elastic plate remains the same as (4.5)

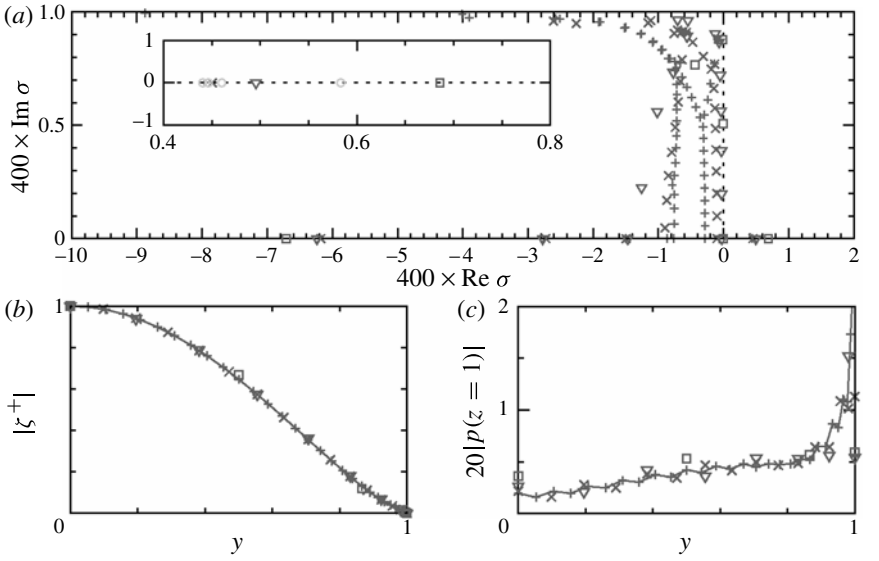

FIGURE 8. (*a*) The spectrum for $\alpha = 0.05$, $k = 1$, $\Gamma^+ = \Gamma^- = 0.5$ and $G = G^- = 0$ using the method described in § 5.2.1. (One very stable stationary mode is omitted to ensure the structure of the continuous spectrum is visible.) The inset highlights convergence for the most unstable mode. Resolutions $M \times N$ are 6×6 (□), 16×10 (▽), 32×12 (×) and 60×20 (+). The inset also has (grey circles) 10×6, 24×10, 40×12 and 80×12. (*b*) Out-of-plane displacement and (*c*) surface pressure profile for the most unstable mode at the four different resolutions.

(modulo the interpretation that, for the elastic case, we consider displacements rather than velocities, and strains rather than strain rates). In contrast to the viscous plate, this state is stable below a non-zero threshold shear. At the onset of buckling, any infinitesimal out-of-plane deflection proportional to $\tilde{H}(y)\mathrm{e}^{\mathrm{i}kx}$ satisfies

$$\frac{8}{3}\frac{1}{\mathscr{S}}\left(\frac{\partial^4\tilde{H}}{\partial y^4} - 2k^2\frac{\partial^2\tilde{H}}{\partial y^2} + k^4\tilde{H}\right) = 4\mathrm{i}k\frac{\partial\tilde{H}}{\partial y},$$

with $\tilde{H} = \partial\tilde{H}/\partial y = 0$ at $y = \pm 1$, yielding an eigenvalue problem for the critical shear strain. This equation is identical to that for the viscous plate on equating the reciprocal shear $1/\mathscr{S}$ with σ. As a consequence, the elastic mode observed at smallest $\mathscr{S}$ is identical in structure and wavelength to the fastest-growing viscous mode.

Appendix C. Numerical method for the Stokes eigenvalue problem

Solving (5.12) numerically is complicated by the boundary conditions at the corners where the vertical walls and free surfaces meet. To validate the method used, we show convergence plots with increasing grid resolutions and provide a discussion of the impact of augmented free-surface boundary conditions and the choice of corner behaviour.

Figure 8 shows convergence of the eigenvalue spectrum with increasing resolution for the augmented boundary conditions used in §§ 5 and 6, together with profiles of

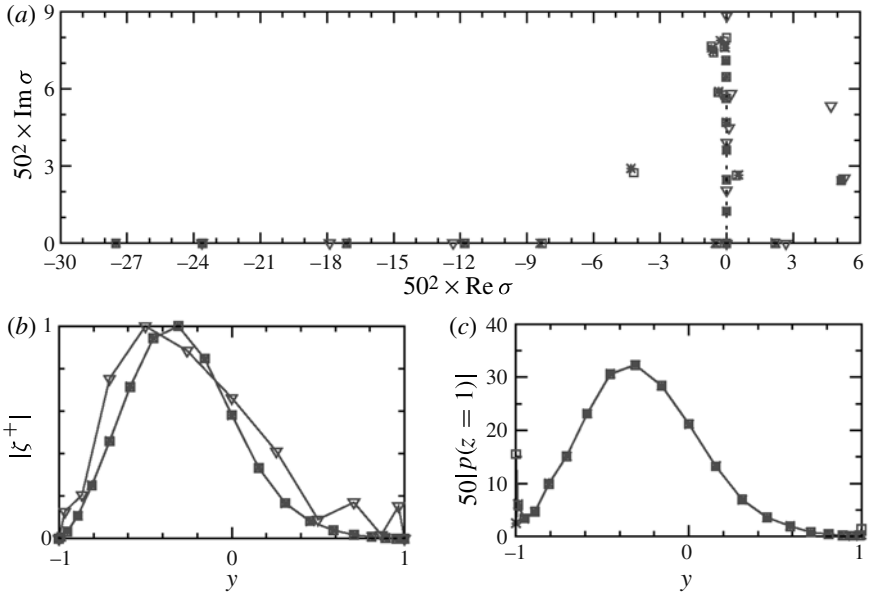

FIGURE 9. As for figure 8 with $k = 8$, $\alpha = 0.02$, $\Gamma^+ = \Gamma^- = 0.5$ and $G = G^- = 0$. Augmented free-surface conditions are: normal component of momentum with corners part of the walls (+); continuity with corners part of the free surface (□); and continuity with corners free (×). All are at 20×10 resolution. Inverted triangles show (v, w) formulation with corners free (pressure plot omitted) at 12×12.

the out-of-plane displacement profile and the pressure on the upper free surface. We note that an apparent pressure singularity appears with increasing resolution.

On solid walls, the appropriate augmented boundary condition is established to be the normal component of the momentum equation (Gresho 1991). However, the choice on the free surface seems less clear. We present results for both the z component of momentum and the continuity condition in figure 9 for the particular set of parameter values of figure 4. We also show results for the corner taken as part of the wall or part of the free surface. The different approaches agree well for the most unstable modes and the most stable modes (i.e. modes far from the continuous spectrum), despite the fairly coarse resolution. With increasing numbers of grid points in each direction, the discrete spectra visually converge to the same values for all choices, and profiles for the pressure, velocity field and out-of-plane displacements all agree. Similarly, using the reduced governing equations obtained by eliminating $\tilde{u}$ and $\tilde{p}$ from (5.12) also yields the same discrete spectrum (although condition number growth prohibited comparison at significantly higher resolution than shown in figure 9). Nevertheless, details of the solutions and spectra at a given resolution are impacted by the choice of discretization procedure on the boundaries. In particular, how well the apparent singularity at the walls is resolved depends on whether the corner is taken to be part of the wall or the free surface. The remaining grid points' values visually appear unaffected. The continuous spectrum is also somewhat sensitive to the choice of augmented boundary conditions: specifically the size of the balloon varies. This balloon appears to be slightly closer to the continuous spectrum at a given resolution for the augmented boundary conditions that we used, motivating our choice.

Appendix D. Short-wavelength approximation for a viscous slab

In the short-wave approximation for the Stokes eigenvalue problem due to Benjamin & Mullin (1988), we assume that it is reasonable to ignore the lateral boundary conditions and thus we Fourier-decompose in y as $\tilde{f}(y,z) = \tilde{\tilde{f}}(z)\,\mathrm{e}^{\mathrm{i}my}$ for cross-sheet wavenumber m. Then the eigenvalue problem (5.12) reduces to

$$\left(\frac{\sigma}{\alpha^2} + \mathrm{i}ky\right)\begin{pmatrix}\tilde{\tilde{H}}\\ \tilde{\tilde{h}}\end{pmatrix} = \boldsymbol{A}\begin{pmatrix}\tilde{\tilde{H}}\\ \tilde{\tilde{h}}\end{pmatrix}, \tag{D 1}$$

where $\tilde{\tilde{H}} = (\tilde{\tilde{\zeta}}^{+} + \tilde{\tilde{\zeta}}^{-})/2$ is the centre-plane deformation, $\tilde{\tilde{h}} = (\tilde{\tilde{\zeta}}^{+} - \tilde{\tilde{\zeta}}^{-})/2$ is the thickness variation and

$$\boldsymbol{A} = \begin{pmatrix} -\alpha\dfrac{4km + c^2(G^- + 2K^2\Gamma)}{4K(sc - \alpha K)} & -\alpha c^2\dfrac{2G - G^- + K^2(\Gamma^+ - \Gamma^-)}{4K(sc - \alpha K)} \\ -\alpha s^2\dfrac{2G - G^- + K^2(\Gamma^+ - \Gamma^-)}{4K(sc + \alpha K)} & \alpha\dfrac{4km - s^2(G^- + 2K^2\Gamma)}{4K(sc + \alpha K)} \end{pmatrix}, \tag{D 2}$$

where $K = \sqrt{k^2 + m^2}$, $s = \sinh(\alpha K)$ and $c = \cosh(\alpha K)$. (These are equivalent to equations (27) and (28) of Benjamin & Mullin (1988).) For our example in figure 5, this translates into sinuous modes having maximum growth rate

$$\mathrm{Re}\,\sigma = -\alpha^3 \max_m \frac{2km + c^2K^2\Gamma}{2K(sc - \alpha K)}, \tag{D 3}$$

and varicose modes, which are much less unstable (none of our modes shown in figure 5 are varicose), having maximum growth rate

$$\mathrm{Re}\,\sigma = -\alpha^3 \max_m \frac{-2km + s^2K^2\Gamma}{2K(sc + \alpha K)}. \tag{D 4}$$

The former have crests aligning with the shear, at roughly 45°, while the latter are anti-aligned.

We include predictions using this approximation in figures 5 and 7.

REFERENCES

BALMFORTH, N. J., CRASTER, R. V. & SLIM, A. C. 2008 On the buckling of elastic plates. *Q. J. Mech. Appl. Maths* **61** (2), 267–289.

BENJAMIN, T. B. & MULLIN, T. 1988 Buckling instabilities in layers of viscous liquid subjected to shearing. *J. Fluid Mech.* **195**, 523–540.

BIOT, M. A. 1961 Theory of folding of stratified viscoelastic media and its implications in tectonics and orogenesis. *Geol. Soc. Am. Bull.* **72** (11), 1595–1620.

BUCKMASTER, J. D., NACHMAN, A. & TING, L. 1975 The buckling and stretching of a viscida. *J. Fluid Mech.* **69** (01), 1–20.

CANUTO, C., HUSSAINI, M. Y. & QUARTERONI, A. 2007 *Spectral Methods: Evolution to Complex Geometries and Applications to Fluid Dynamics*. Springer.

CHAPPLE, W. M. 1968 A mathematical theory of finite-amplitude rock-folding. *Geol. Soc. Am. Bull.* **79**, 47–68.

CHIU-WEBSTER, S. & LISTER, J. R. 2006 The fall of a viscous thread onto a moving surface: a 'fluid-mechanical sewing machine'. *J. Fluid Mech.* **569**, 89–111.

FRIEDRICHS, K. O. & DRESSLER, R. F. 1961 A boundary-layer theory for elastic plates. *Commun. Pure Appl. Maths* **14** (1), 1–33.

GRESHO, P. M. 1991 Incompressible fluid dynamics: some fundamental formulation issues. *Annu. Rev. Fluid Mech.* **23** (1), 413–453.

HOWELL, P. D. 1994 Extensional thin layer flows. PhD thesis, Oxford University.

HOWELL, P. D. 1996 Models for thin viscous sheets. *Eur. J. Appl. Maths* **7** (04), 321–343.

JOHNSON, A. M. & FLETCHER, R. C. 1994 *Folding of Viscous Layers*. Columbia University Press.

MAHADEVAN, L., BENDICK, R. & LIANG, H.-Y. 2010 Why subduction zones are curved. *Tectonics* **29**, article TC6002.

MAHADEVAN, L., RYU, W. S. & SAMUEL, A. D. T. 1998 Fluid 'rope trick' investigated. *Nature* **392**, 140, Addendum and correction, 2000, **403**, 502.

RAMBERG, H. 1963 Fluid dynamics of viscous buckling applicable to folding of layered rocks. *Bull. Am. Assoc. Petrol Geol.* **47** (3), 484–505.

RAYLEIGH, J. W. S. 1945 *Theory of Sound,* vol. II, pp. 313–314. Dover.

RIBE, N. M. 2001 Bending and stretching of thin viscous sheets. *J. Fluid Mech.* **433**, 135–160.

SCHMID, P. J. & HENNINGSON, D. S. 2001 *Stability and Transition in Shear Flows*. Springer.

SILVEIRA, R., CHAIEB, S. & MAHADEVAN, L. 2000 Rippling instability of a collapsing bubble. *Science* **287**, 1468–1471.

SKOROBOGATIY, M. & MAHADEVAN, L. 2000 Folding of viscous sheets and filaments. *Europhys. Lett.* **52**, 532.

SLIM, A. C., BALMFORTH, N. J., CRASTER, R. V. & MILLER, J. C. 2009 Surface wrinkling of a channelized flow. *Proc. R. Soc. Lond.* A **465**, 123–142.

SOUTHWELL, R. V. & SKAN, S. W. 1924 On the stability under shearing forces of a flat elastic strip. *Proc. R. Soc. Lond.* A **105** (733), 582–607.

SULEIMAN, S. M. & MUNSON, B. R. 1981 Viscous buckling of thin fluid layers. *Phys. Fluids* **24**, 1.

TAYLOR, G. I. 1969 Instability of jets, threads, and sheets of viscous fluid. In *Applied Mechanics: Proceedings of 12th International Congress, Stanford University* (ed. M. Hétenyi & W. G. Vincenti), pp. 321–330. Springer.

TEICHMAN, J. A. 2002 Wrinkling and sagging of viscous sheets. PhD thesis, MIT.

TEICHMAN, J. & MAHADEVAN, L. 2003 The viscous catenary. *J. Fluid Mech.* **478**, 71–80.

TIMOSHENKO, S. P. & WOINOWSKY-KRIEGER, S. 1959 *Theory of Plates and Shells*. McGraw-Hill.

TREFETHEN, L. 2000 *Spectral Methods in MATLAB*. SIAM.

YARIN, A. L. & TCHAVDAROV, B. M. 1996 Onset of folding in plane liquid films. *J. Fluid Mech.* **307**, 85–99.